

TESTING THE PRESENCE OF MULTIPLE PHOTOMETRIC COMPONENTS IN NEARBY EARLY-TYPE GALAXIES USING SDSS

SEMYEONG OH^{1,3}, JENNY E. GREENE¹ AND CLAIRE N. LACKNER²

Draft version November 8, 2018

ABSTRACT

We investigate two-dimensional image decomposition of nearby, morphologically selected early-type galaxies (ETGs). We are motivated by recent observational evidence of significant size growth of quiescent galaxies and theoretical development advocating a two-phase formation scenario for ETGs. We find that a significant fraction of nearby ETGs show changes in isophotal shape that require multi-component models. The characteristic sizes of the inner and outer component are ~ 3 and ~ 15 kpc. The inner component lies on the mass-size relation of ETGs at $z \sim 0.25 - 0.75$, while the outer component tends to be more elliptical and hints at a stochastic buildup process. We find real physical differences between the single- and double-component ETGs, with the double-component galaxies being younger and more metal-rich. The fraction of double component ETGs increases with increasing σ and decreases in denser environments. We hypothesize that double-component systems were able to accrete gas and small galaxies until later times, boosting their central densities, building up their outer parts, and lowering their typical central ages. In contrast, the oldest galaxies, perhaps due to residing in richer environments, have no remaining hints of their last accretion episode.

Subject headings: galaxies: elliptical and lenticular, cD – galaxies: evolution

1. INTRODUCTION

In the past ten years, starting with Daddi et al. (2005), there has been an increasing body of work showing that the sizes of massive quiescent galaxies were, on average, significantly smaller than their nearby descendants at fixed mass. While the initial discovery was based on rest-frame UV imaging, the rapid size evolution of early-type galaxies (ETGs) has now been firmly established in the rest-frame optical using near-infrared imaging (Trujillo et al. 2006; Zirm et al. 2007; Toft et al. 2007; Stockton et al. 2008; McGrath et al. 2008) and extended to large (Buitrago et al. 2008) and spectroscopic (van Dokkum et al. 2008; Damjanov et al. 2011; van de Sande et al. 2011) samples. Recently, van der Wel et al. (2014) confirmed that the mass-size relation of ETGs evolves rapidly over $0 < z < 3$ using a large, spectroscopic sample from multiple fields.

Generally, this dramatic size evolution has been taken to mean that individual massive quiescent galaxies have grown in size over the past ~ 10 Gyr. So far, there is no convincing observational evidence for a substantial population of compact quiescent galaxies in the local universe at matching number density as the high- z samples (Trujillo et al. 2009; Taylor et al. 2010), although ongoing searches for such galaxies both nearby and at intermediate redshift may change this picture (e.g., Valentinuzzi et al. 2010; Poggianti et al. 2013; Damjanov et al. 2014; Saulder et al. 2015). The compact galaxies at high redshift must have grown in size to transform into galaxies seen in the local universe. Because the high- z compact galaxies are often quiescent, they are naturally imagined

to be the progenitors of present day ETGs, implying a significant size evolution (although see also Graham et al. 2015).

Alternatively, if increasingly large star-forming galaxies add to the population of ETGs on the red sequence at later times, it is possible that size evolution may appear more dramatic than it truly is for individual systems (e.g., Cassata et al. 2013; Carollo et al. 2013; Newman et al. 2012). Disentangling the effect of this so-called progenitor bias from intrinsic size growth is a challenging task and is actively under debate. If the progenitor bias is a more prominent cause of the size evolution, on the one hand one expects to find some of the undisturbed old, compact, and red galaxies in the nearby universe as mentioned above. On the other hand, we also expect to find consistently younger ages for larger ETGs which joined the population at later times. The recent study of Keating et al. (2015) looked at the stellar populations of $0.5 < z < 1.4$ ETGs as a function of their size and found interesting morphology-dependent trends (Graves et al. 2009b; Valentinuzzi et al. 2010).

If there is indeed intrinsic size growth of compact red galaxies at $z \lesssim 2$, what drives the evolution? Several theoretical scenarios have been proposed to explain the observed size evolution including major (Boylan-Kolchin et al. 2006; Hopkins et al. 2009) and minor mergers (Naab et al. 2009; Hopkins et al. 2010), or adiabatic expansion due to AGN feedback (Fan et al. 2008). One favored theory to explain such size evolution is a two-phase formation of ETGs (Naab et al. 2009; Oser et al. 2010). In this scenario, a massive compact core forms predominantly in situ through early star formation ($z > 3$) and then in the second phase grows by the dissipationless accretion of smaller galaxies over an extended period of time, which accumulates mass in the outskirts and increases the size rapidly ($R_e \propto M_*^\alpha$ where $\alpha > 1$). A pure dry merger scenario, however, is challenged by the lack of observed

¹ Department of Astrophysics, Princeton University, Princeton, NJ 08544, USA

² Kavli Institute for the Physics and Mathematics of the Universe (WPI), Todai Institutes for Advanced Study, the University of Tokyo, Kashiwa, Japan

³ semyeong@astro.princeton.edu

satellite galaxies to match the size evolution (Newman et al. 2012) and the non-evolving density slope of ETGs measured from stellar kinematics and gravitational lensing (Sonnenfeld et al. 2013). Recent cosmological simulations also find that the evolutionary path taken by compact, massive galaxies at $z \approx 2$ can lead to a variety of outcomes (Wellons et al. 2016). While about half of these systems form the centers of more massive galaxies today, some are completely disrupted, and others remain compact, with some dependence on the environment.

In light of these recent developments, it is interesting to revisit studies of the surface brightness profiles of local ETGs, although traditionally they are often regarded as smooth and well-described by a single photometric component. If the present day ETGs are indeed formed in a two-phase scenario, one may be able to see changes in the surface brightness profile where the outskirts were built up via minor mergers.

Several recent studies have performed multi-component fitting to early-type galaxies in a similar context. Huang et al. (2013b) analyzed optical images of 94 nearby early-type galaxies, and argued that the majority of these galaxies in fact require three components to fully describe their two-dimensional surface brightness profile. They further related the photometric substructure to a two-phase formation scenario by comparing the mass-size relation and the surface brightness profiles of the subcomponents with high- z compact red galaxies (Huang et al. 2013a), and argued that the decomposition reveals a fossil record of mass accumulation on the outskirts of “red nuggets” at high redshift.

D’Souza et al. (2014) also searched for faint stellar halos around isolated central galaxies (not necessarily of early-type) by stacking aligned galaxy images in bins of stellar mass and concentration. The highest concentration, most massive galaxies in their study (most relevant to our work) show a stellar halo reaching to radii of ~ 100 kpc and a surface brightness below 30 mag arcsec $^{-2}$. In their stacked images, the stellar halos comprise a progressively larger fraction of the total flux, and become more elliptical, as the stellar mass increases. Finally, Meert et al. (2015) performed multiple two-component fits to the SDSS spectroscopic sample, yet focused on providing consistent and accurate size or magnitude measurements across galaxies of varying luminosity and morphological types rather than attaching physical meaning to subcomponents, aside from noting that the classical bulge+disk interpretation is probably not valid for the two component galaxies at the brightest end. These studies have not yet explored any connection between the profile shapes and galaxy stellar populations.

We note that the operating definition and selection of ETGs varies between the studies discussed above. At high redshift, selections are often based on galaxy color (e.g., Toft et al. 2007; Trujillo et al. 2006; Zirm et al. 2007; van der Wel et al. 2014) or Sersic index (Bell et al. 2012), while at low redshift visual morphology, emission line strength, and/or concentration could all be employed as well as color. The selection of ETGs based on different galaxy properties may lead to different galaxy samples with varying degrees of contamination from star-forming galaxies (Moresco et al. 2013). In fact, Keating et al.

TABLE 1
SUMMARY OF SAMPLE SELECTION

Condition	Count
Parent sample (Nair & Abraham 2010)	14034
E/S0 without warnings	2497
No pair/disturbed/tail/AGN flag with $\sigma > 70$ km/s	1365
Valid physical parameters	1134
Good cutout images	877
Further visual inspection & cutout image requirement	838

(2015) found that subtleties in the sample selection of ETGs may lead to different conclusions about the importance of progenitor bias. When ETGs are selected by color and bulge-to-total ratio only, massive compact ($R_e < 2$ kpc) ETGs are younger than their larger counterpart, suggesting that the progenitor bias is not the main driver of the size evolution. However, when an additional morphological criterion of smoothness (Simard et al. 2002) is included, the outcome is reversed.

Taking the idea that the compact, red galaxies at high redshift may evolve to be nearby passive, quiescent ETGs, we examine the photometric structure of morphologically selected ETGs, including morphological ellipticals with blue colors due to ongoing star formation. We thus decompose a nearby sample of morphologically selected early-type galaxies into two photometric components, envisioned to be a core that may have formed in an early dissipational process and an outer component. For the first time, we also test for a relationship between stellar population ages and multi-component structural fits.

The plan of the paper is as follows. We describe the sample and data in §2, and justify our fitting method and model selection in §3. We present the results in §4 and end with the summary and discussion in §5. Throughout the paper, we adopt the concordance cosmological parameters $H_0 = 70$ km s $^{-1}$ Mpc $^{-1}$, $\Omega_M = 0.3$, $\Omega_\Lambda = 0.7$.

2. SAMPLE & DATA

We describe our sample selection and data used to construct cutout images for fitting, which is summarized in Table 1. We use the detailed visual morphology classification catalog of Nair & Abraham (2010) to construct a sample of nearby elliptical galaxies in a range of mass and environment. The catalog is based on the SDSS DR4 main spectroscopic sample, and extends to $z = 0.1$ in order to include the most massive galaxies, which match most closely the mass of high redshift compact galaxies. We select unambiguously identified RC3 Hubble types of cD, E, and E/S0 (TType = -5 , flag on Ttype = 0). Of the 2497 galaxies fitting these criteria, we remove galaxies flagged for disturbed morphology by selecting those with disturbed flag = 0, and additionally inspect SDSS images visually to remove galaxies showing any morphological peculiarities. We also remove any galaxies with a close “companion” in the image (Pair = 0 and Pair flag type = 0) e.g., an overlapping star, for the same reason. We exclude galaxies harboring AGNs according to the classification scheme of Kewley et al. (2001) and Kauffmann et al. (2003b) if this information is available. We require that galaxies have valid velocity dispersion measurements ($\sigma > 70$ km s $^{-1}$), stellar masses from Kauff-

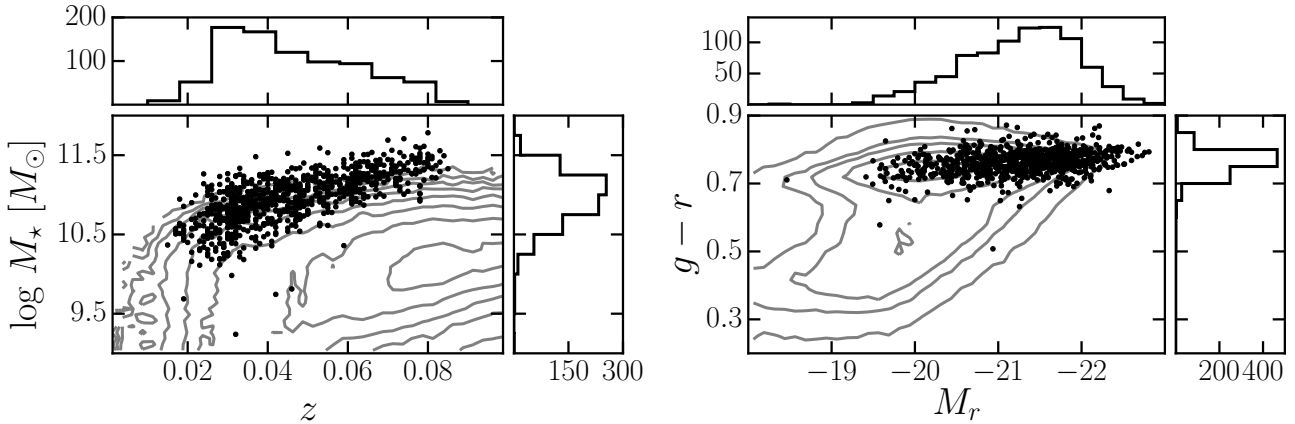


FIG. 1.— Distribution of the sample galaxies (black dots) in the redshift vs. $\log M_*$ plane (left) and $(g-r)$ vs. M_r color-magnitude diagram (right). In each panel, we show the distribution of SDSS galaxies in the NYU-VAGC (Blanton et al. 2005) at $z < 0.1$ as gray contours with logarithmic spacing. Histograms show the distribution of each parameter for the sample only.

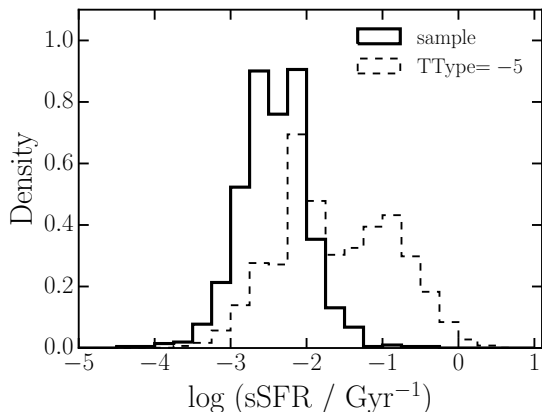


FIG. 2.— Density histogram of specific star formation rate of the sample. These values are derived from H α emission and color in Brinchmann et al. (2004). We show the distribution for all TType = -5 galaxies in Nair & Abraham (2010) for comparison. The galaxies in our sample have very low specific star formation rates, and does not include morphological ellipticals with specific star formation rate larger than 0.1 Gyr^{-1} .

mann et al. (2003a), group halo masses from Yang et al. (2007) and an estimate of the environment (Baldry et al. 2006). We are left with 1134 elliptical galaxies that make these cuts.

We use the SDSS r -band corrected frame images for surface brightness profile fitting. These images have been sky-subtracted by fitting a smooth spline model, an improved method of estimating global sky background compared to the previous PHOTO sky estimates (see Blanton et al. 2011, for details). For the fitting, we cut out frame images centered on each target galaxy with a size of 40 petrosian radii following Meert et al. (2013). We require that more than 70% of the desired cutout size be covered in a single SDSS frame image. We use *Source Extraction and Photometry in Python (SEP)*⁴ to make an object mask for each image. We mask all neighboring objects of the target galaxy when fitting. As the central part of the galaxy is important for surface brightness profile fitting, we further require that no more than 10%

of the area in concentric circles of radius 5, 10, 20, 50 pixels from the center be masked. Point spread function (PSF) images for PSF-convolution are read from SDSS psField files at the position of each galaxy using the SDSS readPSF tool. We visually check the integrity of the remaining 877 galaxies with good cutout images that satisfy the aforementioned requirements using SDSS color composite images, and exclude a small number of galaxies that are not elliptical galaxies, or that suffer from artificial or astrophysical defects in their images (Table 1).

Our final sample with good cutout images comprises 838 elliptical galaxies. Our sample spans a redshift range of $0.015 < z < 0.085$ and a stellar mass range of $\log(M_*/M_\odot) = 9.24$ to 11.78 (Figure 1). Although we do not specifically place a lower limit on stellar mass, we note that 75% of our sample galaxies have $\log M_* > 10.75 M_\odot$. This corresponds to the stellar-mass limit that significantly reduces contamination in early-type samples from star-forming galaxies when using e.g., morphology to select ETGs (Moresco et al. 2013). Indeed, most of the galaxies in our sample fall on the red sequence in the $(g-r)$ vs M_r color magnitude diagram (right panel of Figure 1). We also investigate the specific star formation rates (sSFR), as measured from H α emission and color (Brinchmann et al. 2004). The specific star-formation rates for our sample galaxies are low (Figure 2), with 86% of the sample below 0.01 Gyr^{-1} . We note that of 5321 passive galaxies with $\text{sSFR} < 0.01 \text{ Gyr}^{-1}$ in Nair & Abraham (2010), 46% are ellipticals (TType = -5). On the other hand, compared to all E/S0's visually classified by Nair & Abraham (2010) (dashed line in Figure 2), the galaxies in our sample correspond to the most quiescent galaxies, and exclude E/S0's with specific star formation rate higher than 0.1 Gyr^{-1} .

3. FITTING

In this section, we describe our fitting procedure, including our choices of model profiles and the fitting method (§3.1), model selection (§3.2) and the effects of PSF and residual sky background to the fitting (§3.3).

3.1. Fitting Procedure

⁴ <https://github.com/kbarbary/sep>

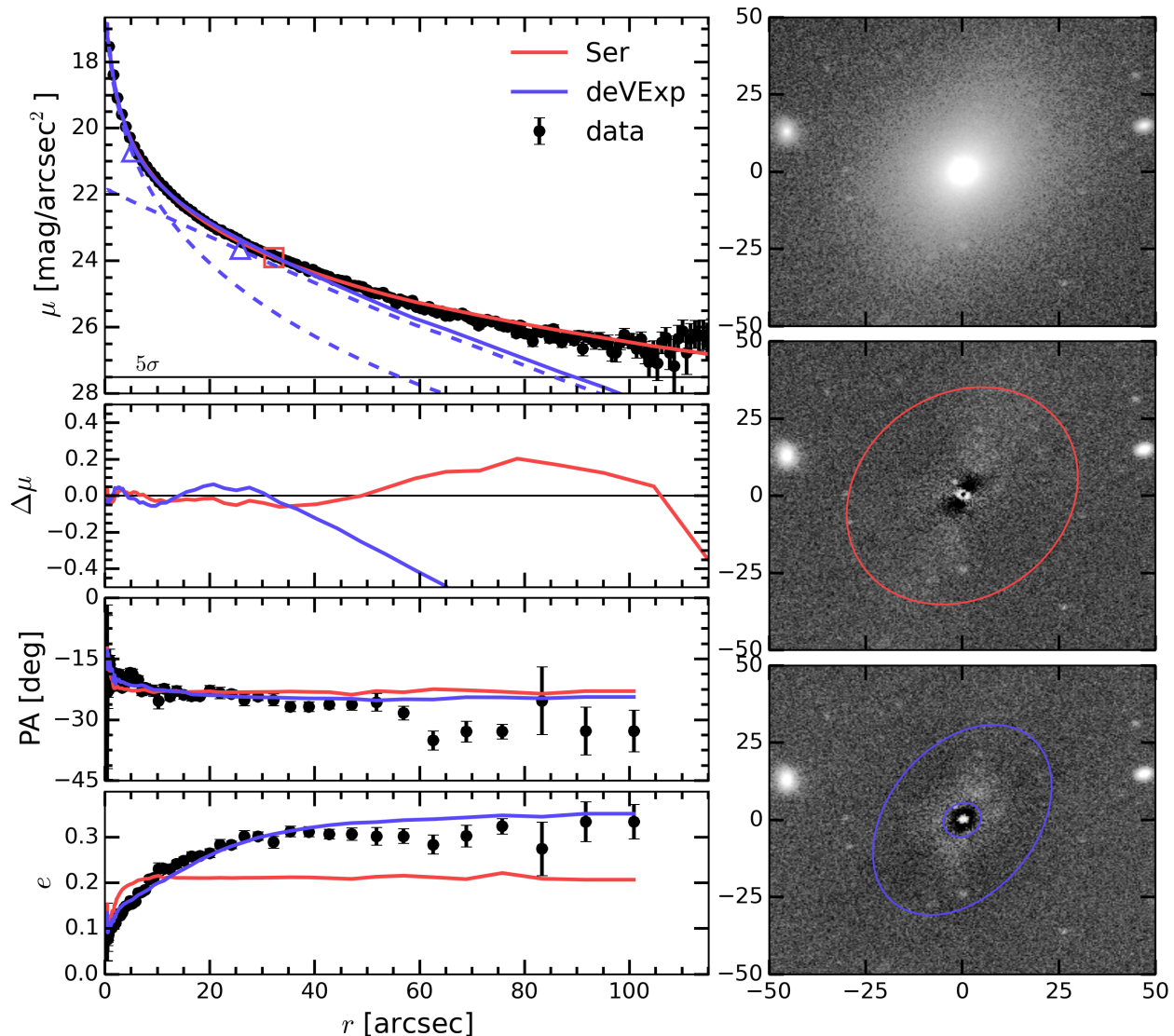


FIG. 3.— Example of a double component ETG selected with high confidence ($\Delta\chi_e^2 > 200$, sample id = 15). On the left, we show the azimuthal surface brightness profiles, residuals, PA, and ellipticity from top to bottom as a function of radius from the galaxy center for data (black circles) and two models, the single Sérsic (red) and deVExp (blue). On the top left panel, two blue dashed lines for deVExp model indicates the deV and Exp components respectively. For each subcomponent of the models, we indicate R_e with markers of the same color. The horizontal line corresponds to the 5σ surface brightness limit. On the right, we show the galaxy image, and the residual images of the best-fit single Sérsic and deVExp model from top to bottom. The ellipses on the residual images indicate the effective ellipse for each component of the model.

We perform two dimensional image fitting using a combination of Sérsic models (Sérsic 1968; Graham & Driver 2005)

$$I(R) = I_e \exp\left(-b_n[(R/R_e)^{1/n} - 1]\right) \quad (1)$$

where the geometric shape of the isophotes are assumed to be ellipses described by a center, position angle (PA), and ellipticity. The ellipticity is defined as $1 - b/a$ where b/a is the minor-to-major axis ratio of the ellipse. Here, R_e is the effective radius, I_e the effective surface brightness, and n the Sérsic index. The constant b_n is chosen such that half of the total flux is enclosed within R_e . The allowed range of the Sérsic index n is between 0.1 and 9.

We first perform the single Sérsic model fitting as a reference. The two component model is a sum of a de

Vaucouleurs and an exponential with Sérsic indices of $n = 4$ and $n = 1$ respectively (hereafter deVExp). The two components share a common center, but are allowed to have different PA and ellipticity. We choose to fix the Sérsic indices of the two component model to minimize degeneracy between index and size in Sérsic models (e.g., Kormendy et al. 2009), and place the sizes of each component among galaxies on equal footing. Our goal is not to find the *best* model for the surface brightness of each galaxy. Rather, we use the double component model to test whether a two-component decomposition is justified. We find that this double component modeling is a convenient way to see if changes in profile shape require this decomposition. We are motivated to use the exponential ($n = 1$) profile for the outer part since it is flat, making it

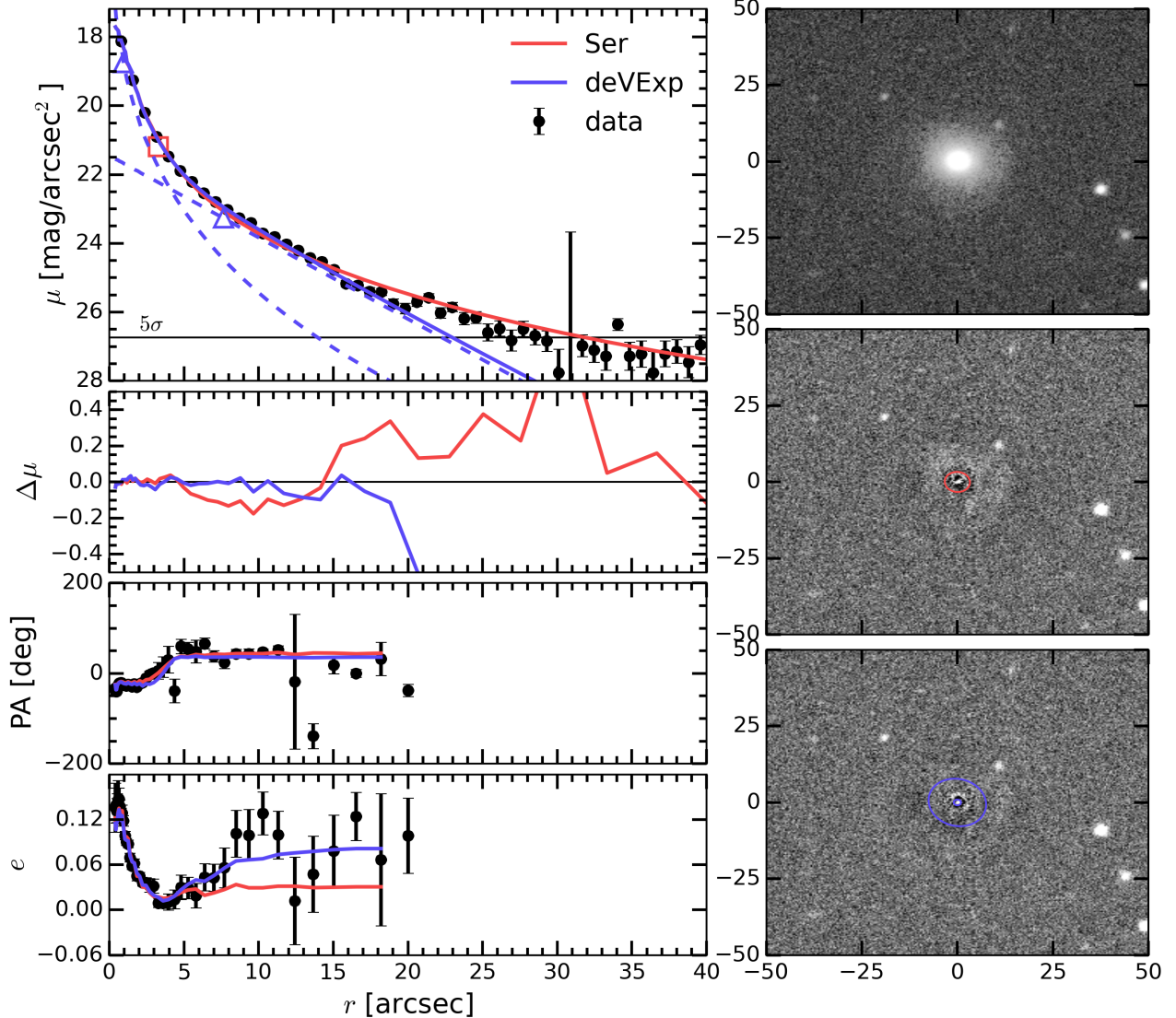


FIG. 4.— Same as Figure 3 but for a double component ETG with $\Delta\chi_e^2 < 200$ (sample id = 188). At $r > 20$ arcsec, the data are of insufficient signal-to-noise ratio to constrain PA and ellipticity.

less degenerate with the profile of the inner component. We further discuss our choice of indices and the effect of freeing them in §4.2.

We use IMFIT, a flexible galaxy image fitting tool (Erwin 2015). To find the best-fit model of a given functional form for each galaxy, we minimize the residual sum of squares using the Levenberg-Marquart gradient search algorithm. Residuals are weighted by $1/\sigma_i$, where σ_i is the error at each pixel, obtained from the SDSS frame images. For the deVExp model, a choice of initial parameters may be important in reaching optimal parameters. While this algorithm only guarantees a local minimum, we sample a grid of reasonable initial conditions to make sure that we obtain the best model possible within the parameter space of our interest.

First, we fit a single de Vaucouleurs model. We use its parameters as a reference for the deV component of the deVExp model. The initial parameters for the one-component fit are set using the existing information

on Petrosian half light radius and axis ratio from Nair & Abraham (2010). While the true best-fit de Vaucouleurs of the final deVExp model may change, the single-component fit still serves as a good starting point. Second, we fit the deVExp model with an array of starting parameters. Given the best-fit parameters $R_{e,\text{deV}}$, $I_{e,\text{deV}}$, PA_{deV} , e_{deV} of the single deV model, we explore a grid of flux ratios $F_{\text{Exp}}/F_{\text{tot}} = 0.1, 0.5, 0.9$ and size ratios $R_{e,\text{Exp}}/R_{e,\text{deV}} = 1, 5, 10$. In each of the nine combinations of these two parameters, we try $\Delta\text{PA} = 0$ (parallel) and 90 (orthogonal). We also try two different initial ellipticities of 0.1 and 0.5 for the newly added Exp component. This grid of values results in 36 different initial conditions in flux ratio, size ratio, PA difference, and ellipticity. After optimizing the model from this set of initial conditions, we choose the one with the minimum best-fit chi-square value as our best-fit deVExp model for each galaxy.

The azimuthal light profiles of nearby elliptical galax-

ies are generally known to be well described by a single Sérsic model (Sérsic 1968; Caon et al. 1993; Kormendy et al. 2009). Indeed, it is this flexibility that makes the Sérsic model excel in fitting galaxy images, when accurately describing the photometric substructure is not warranted (e.g., due to lack of resolution), or not of interest. However, the definitive characteristic of a two-component model that the single Sérsic fails to capture is any change in isophotal shape reflected in e.g., PA or ellipticity as a function of radius. This has already been noted by e.g., Huang et al. (2013b) and D’Souza et al. (2014), and was one of their main reasons to prefer a multi-component model.

Adding the second (Exp) component, we find that the deVExp model adequately describes the observed large scale shifts in isophotal shape. In many cases the single-component fit fails to capture these changes. However, we often find that the deVExp model systematically fails to account for the outermost light profile. Usually the observed light profiles decline more slowly than an exponential, typically at $\mu \lesssim 26$ mag arcsec $^{-2}$ and $r > 40$ arcsec.

We show examples of “double component ETGs” that we determine are better fit by the two-component model (deVExp), and we specify the criteria below. Figure 3 is an example of a double component ETG that we dub high confidence because the large shift in ellipticity is much better captured in the deVExp model. The azimuthal surface brightness profile extends down to 26 mag arcsec $^{-2}$, and is well described by a single Sérsic. However, this model fails to reproduce the ellipticity curve. The ellipticity profile of the galaxy continues to rise to $e \sim 0.3$ at $5 < r < 30$, while the Sérsic model locks onto a value close to the best-fit ellipticity. This is typical of single Sérsic model ellipticities modulo some variation in the central region (< 5 arcsec) due to the PSF. In fact, one can see a hint of elongated low surface brightness light in the residual image of the Sérsic model (middle panel of the right column in Figure 3). The two component deVExp model, on the other hand, can match the ellipticity profile by adjusting the outer Exp component to have a higher ellipticity than the inner deV. As discussed earlier, the decline in the surface brightness profile at the very faint end is not as steep as exponential, and the deVExp model fails at the largest radii. Considering only the 1D surface brightness profile, one might think that the deVExp model could be improved by increasing the R_e of both components. However, in 2D fitting, the change in isophotal shape naturally demands the arrangement of each component to simultaneously match the ellipticity and PA profiles.

Figure 4 shows an example double component ETG with a modest change in ellipticity. The general characteristics are similar. Note that the non-trivial change in PA and ellipticity in the inner $\lesssim 4$ arcsec due to PSF is quite well matched between the data and the PSF convolved models.

3.2. Model Selection

With this in mind, we now turn to model selection between the single Sérsic and the deVExp model. Model selection is not an easy task in general, and there is no absolute way to solve all model selection problems. Even in galaxy surface brightness fitting alone, we see a variety

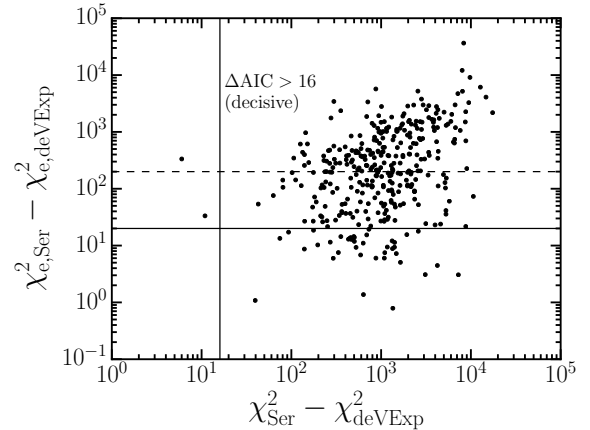


FIG. 5.— Correlation between the difference in χ^2 and χ_e^2 for ETGs not excluded by the conditions on Table 2. The vertical line is a formal limit to prefer the deVExp model according to the Jeffreys’ scale (See § 3.1 for a description). The solid (dashed) horizontal lines correspond to cuts for the assignment of double component (HC) ETGs. Note that the 65 (17%) and 26 (12%) of double and double HC ETGs for which the χ^2 of deVExp model is increased relative to the Sérsic model are not shown.

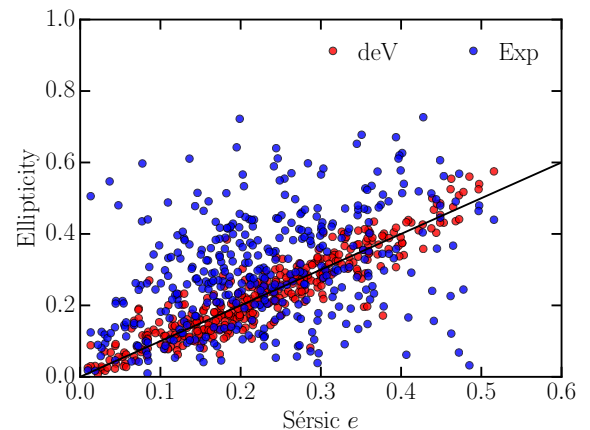


FIG. 6.— Component ellipticity vs. single Sérsic ellipticity for double component ETGs. Red and blue circles correspond to the deV and Exp ellipticity of the best-fit deVExp models.

of criteria adopted in recent studies:

- Lackner & Gunn (2012) use the F -distribution expected from the difference of χ^2 to test the existence of a bulge component in addition to an exponential disk although the model is non-linear.
- Huang et al. (2013b) selects models with the minimum number of components that are “visibly distinct”, which primarily means that not only the 1D surface brightness profiles but also the shapes (ellipticity and PA) of isophotes should be recovered.
- Meert et al. (2015) uses an independent flagging system to place each galaxy into four categories, one of which is a two component galaxy. The final reliable two-component galaxies are those with “intermediate bulge-to-total ratio and reasonably well-behaved subcomponents”. They, however, did not argue for a strong physical interpretation of the two component early-type galaxies.

- D’Souza et al. (2014) employed a Bayesian framework, and used a nested sampling algorithm to compute the Bayes factor when comparing single to multi Sérsic models for their stacked aligned images.

Perhaps the most conceptually straightforward and appealing approach would be to do both parameter estimation and model selection with a Bayesian framework. However, this comes at the cost of considerable additional computing power. We instead come up with a set of objective criteria that are relatively simple to compute yet still take advantage of the two dimensional fitting that we perform. First, we discard the deVExp model if the R_e of the Exp component is smaller than that of the deV, or is beyond the image size, in which case it is fitting the small residual background. Second, we require that the exponential component dominates the surface brightness profile of the galaxy somewhere over the observed radial range.

Finally, to select galaxies for which any change in isophotal shape is better captured by the deVExp model, we compute the residual sum of squares for each model from the ellipticity profiles. We use the IRAF ellipse task to fit the isophotes of galaxies with ellipses as a function of semi-major axis for the data and both models. Using IRAF ellipse, we are able to measure the PA and ellipticity down to a mean surface brightness of $25.3 \text{ mag arcsec}^{-2}$, at which the signal-to-noise ratio is typically 25. Below this threshold, the shape is unconstrained by the current data due to decreased signal-to-noise. We quantify the goodness of fit of each model in describing the ellipticity curves as:

$$\chi_e^2 = \sum_a \left(\frac{e_{\text{data}}(a) - e_{\text{model}}(a)}{\sigma_{e, \text{data}}(a)} \right)^2 \quad (2)$$

where the summation is over the entire semi-major axis range, and the radial binning of the data and the models are identical. The meaningful quantity is the difference in χ_e^2 between the single Sérsic and the deVExp model, $\Delta\chi_e^2 = \chi_{e, \text{Ser}}^2 - \chi_{e, \text{deVExp}}^2$.

After visual inspection of the residual images, the azimuthal surface brightness profiles, and the PA and ellipticity profiles, we come up with an empirical cut to select “double component” galaxies where the deVExp model significantly improves the fit to any change in shape. We prefer the deVExp model for any galaxy where $\Delta\chi_e^2 > 20$, and call this group double component ETGs. We keep a subset of this group with a higher $\Delta\chi_e^2$ threshold of 200 ($\chi_e^2 > 200$) as high confidence (double HC) to assess the validity of our results on double component ETGs with a more conservative subsample. Table 2 summarizes our model selection process with the number of galaxies flagged for each condition.

Although we select double component ETGs by χ_e^2 , we note that in the majority of cases, the total χ^2 is also significantly reduced beyond the level that formally may be attributed to the increased degree of model complexity. Figure 5 shows the distribution of the difference in the total chi-square, $\Delta\chi^2 = \chi_{\text{Ser}}^2 - \chi_{\text{deVExp}}^2$, versus the difference in χ_e^2 for those not excluded by the conditions on Table 2. The strong correlation indicates that the improvement in the double component model is accompa-

TABLE 2
SUMMARY OF MODEL SELECTION

Condition	Count
Total	838
a. $R_{e, \text{Exp}}$ outside of image	45
b. $R_{e, \text{Exp}} < R_{e, \text{deV}}$	94
c. Exp subdominant everywhere	263
Not excluded due to a, b, c	526
$\Delta\chi_e^2 > 20$ (double)	388
$\Delta\chi_e^2 > 200$ (double HC)	220

nied by improvement in fitting the change in ellipticity. We use the Akaike Information Criteria (AIC; Akaike 1974) to demonstrate the improvement in χ^2 . Under the assumption that the noise is normally distributed, the AIC is related to χ^2 through $\text{AIC} = 2k + \chi^2$ where k is the number of free parameters in each model (only differences in the AIC are meaningful, not the absolute value). According to the Jeffreys’ scale (Jeffreys 1961), one may take $\Delta\text{AIC} > 10$ as strong evidence to prefer the more complex model that reduces χ^2 . Since the deVExp model has three additional free parameters, the formal cut to decisively prefer a deVExp model to the single Sérsic is 16, which we show as a vertical line in Figure 5. We note that 83% (88%) of our double component (HC) ETGs satisfy this criterion, with most exceeding the cut by a large margin.

As already noted, often the azimuthal surface brightness profile of ETGs falls off less steeply than exponential, which will tend to decrease $\Delta\chi^2$. Thus, only when there is a greater improvement in fitting the overall surface brightness at $\mu \gtrsim 25 \text{ mag arcsec}^{-2}$, will the $\Delta\chi^2$ will be positive by a large margin. Furthermore, it is worth noting that $\Delta\chi_e^2$ correlates with $\Delta\chi^2$, hinting at a relation between capturing the isophotal shape and the decrease in χ^2 . We also note that in 17% (12%) of double component (HC) ETGs, χ^2 is actually increased for the deVExp model, perhaps expected from the occasional failure to fit the outer isophotes and the flexibility of the Sérsic models. We nevertheless include these in our double component ETGs for consistency.

Figure 6 compares the ellipticity of the deV and Exp components with the ellipticity of the single Sérsic model for each galaxy. It is clear that the inner deV components have almost identical shape as the single Sérsic. In fact, the difference in the ellipticity of the inner deV and that of the single Sérsic is mostly below 0.05. This difference is expected since a single component model will try to fit the shape of the central part of the galaxy where the signal-to-noise is the highest. On the other hand, the outer Exp component is uncorrelated with the inner shape. This argues that we are not just dividing a single Sérsic into two but actually fitting outer light profiles of different shapes. It is also apparent from this figure that the outer component tends to be more elongated than the inner component. We revisit the ellipticity distribution of the subcomponents in §4.

We provide the derived structural parameters from the single Sérsic and deVExp model (for double component ETGs) with other basic properties of the sample in Table 3.

TABLE 3
STRUCTURAL PARAMETERS OF BESTFIT MODELS

Column name	Description
ID	Unique sample ID
Name	SDSS name
RA	Right Ascension (J2000)
DEC	Declination (J2000)
z	Redshift
σ	Velocity dispersion in km s^{-1}
M_r	Absolute r -band magnitude
$g - r$	Rest-frame $g - r$ color
FWHM_{psf}	Full-width at half maximum of the PSF in arc seconds
n_{Ser}	Sérsic index for single Sérsic model
e_{Ser}	Ellipticity of single Sérsic model
f_{Ser}	Flux of single Sérsic model in magnitudes
$R_{e,\text{Ser}}$	Effective radius of single Sérsic model in arc seconds
flag	Flag on double component ETGs: 2 for high-confidence ($\Delta\chi_e^2 > 200$) double component, 1 for double component with $20 < \Delta\chi_e^2 < 200$, and 0 for single component ETGs
e_{deV}	Ellipticity of the deV component of deVExp model
PA_{deV}	Position angle of the deV component of deVExp model in degrees
$R_{e,\text{deV}}$	Effective radius of the deV component of deVExp model in arc seconds
f_{deV}	Flux of the deV component of deVExp model in arc seconds
e_{Exp}	Ellipticity of the Exp component of deVExp model
PA_{Exp}	Position angle of the Exp component of deVExp model in degrees
$R_{e,\text{Exp}}$	Effective radius of the Exp component of deVExp model in arc seconds
f_{Exp}	Flux of the Exp component of deVExp model in arc seconds

NOTE. — Table 3 is published in its entirety in the electronic edition of the Astrophysical Journal. A portion is shown here for guidance regarding its form and content.

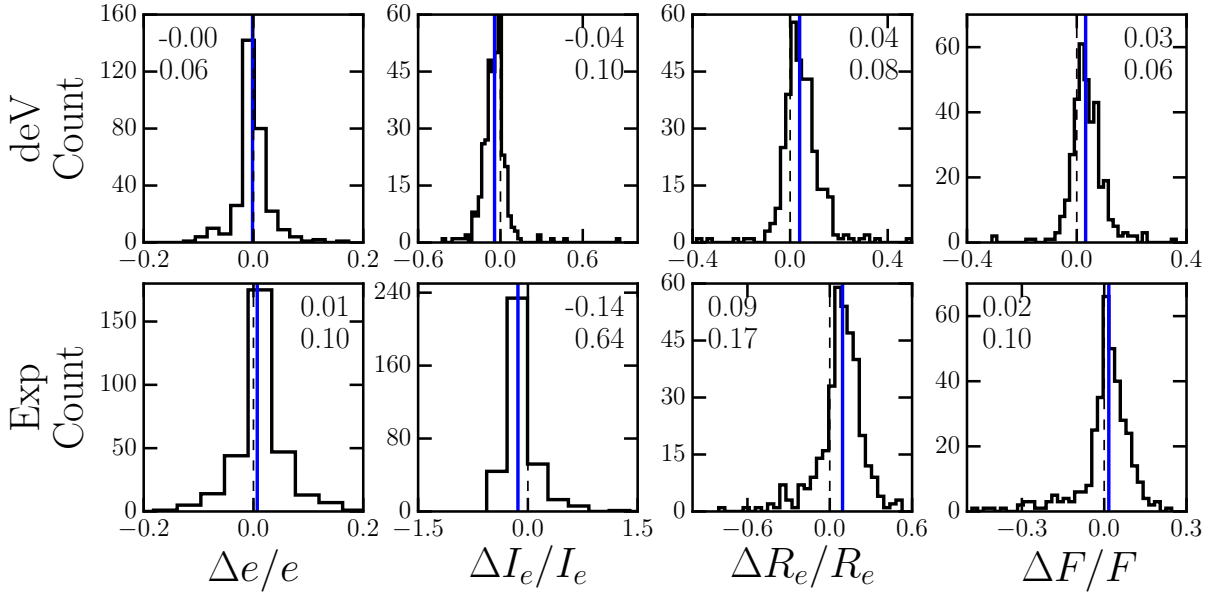


FIG. 7.— Histogram of fractional difference in key parameters of the best-fit deVExp model with and without a fixed residual sky component. The top and bottom rows show the distribution for the inner deV and the outer Exp component respectively. From left to right, the parameters are ellipticity, effective surface brightness, effective radius, and total flux. In each panel, the mean and the standard deviation of the distribution are quoted. The black dashed line and blue solid line indicate zero and the median respectively.

3.3. Systematic Uncertainty From Residual Sky and PSF

The dominant potential sources of systematic uncertainty derive from errors in sky subtraction and the PSF model. We briefly discuss the effect of each to our selection and parameter estimation of double component ETGs.

As described in Section 2, we adopt sky-subtracted frames from the improved algorithm of Blanton et al. (2011); here we only test the impact of small errors in

that sky value. To test the effect of any residual sky, we first estimate the residual by adding a flat sky component to the single Sérsic model. We find that the magnitude of any residual sky brightness in our cutout images is less than $25 \text{ mag arcsec}^{-2}$ and peaks around $27.5 \text{ mag arcsec}^{-2}$. We then add this value as a fixed flat sky component in our modeling, and re-fit the deVExp model to see whether our component determination changes. We use the previously obtained best-fit parameters as the initial guess.

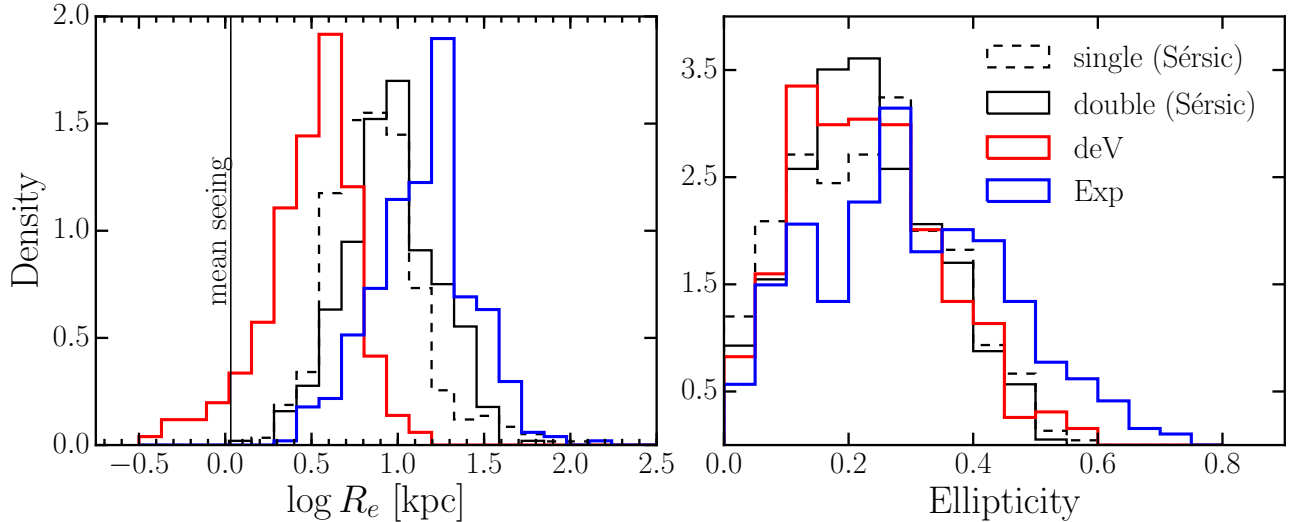


FIG. 8.— Distribution of size and ellipticity for single and double component ETGs. We present the effective radius and ellipticity measured using the single Sérsic model for single and double component ETGs in black, dashed, and solid lines respectively. For double component ETGs, we also show the distribution in R_e and ellipticity measured for the deV (red) and Exp (blue) lines separately in the deVExp model. On the left panel, the vertical line marks the mean physical size corresponding to the seeing for the sample.

Only a small fraction ($\lesssim 10\%$) of our initial assignment to single or double component ETGs change characterization when we change the sky level. Of 388 (220) double component (HC) ETGs (Table 2), 35 (23) are excluded, and 25 (15) are added when putting in a fixed flat sky component. Given that this fraction is so small, we conclude that residual sky errors do not impact our conclusions. For simplicity, we maintain our original classifications, but this test tells us that the systematic errors in sky level do not impact our conclusions.

We also investigate how much the key fit parameters of each subcomponent change due to sky errors using the subset of double-component galaxies with robust classification. Figure 7 shows the distribution of the fractional differences in ellipticity, effective surface brightness, effective radius, and total flux for the deV (top) and Exp (bottom) component. We find the position angle virtually unchanged, and omit this from the figure. The median of the distribution is marked with a blue line, and its numerical value is indicated in each panel along with the standard deviation.

The ellipticities of the subcomponents are robust against any residual sky, although the Exp shows the largest scatter. Adding in a fixed sky has little effect on the inner deV profile, resulting in an overall uncertainty of $\lesssim 10\%$ (1σ). Unsurprisingly, the parameters of the outer Exp component show larger deviations when a fixed sky component is included. The profile moves systematically towards a slightly fainter but larger component. Although the I_e and R_e of individual Exp components may vary by $\approx 20\%$ or more, we find that the total flux in the Exp component is much more robust (column 4 in Figure 7). The systematic errors due to sky presented here are dominant over statistical errors. We estimate the errors in the parameters of either the single Sérsic or deVExp models from the standard deviations of the distribution of fractional difference in each parameter between the model with no sky and the model with a fixed flat sky. For example, we estimate the error

on R_e of the deV component in the deVExp model to be 8% (Figure 7).

Our selection of double component ETGs is unaffected by small uncertainties in the PSF model. The mean FWHM of the PSFs for the sample is 1.19 ± 0.2 arcsec. We note that only 29 double component ETGs have an inner deV component that is only marginally resolved ($R_e < 1.5 \times$ FWHM of the PSF). As we show in 4.1, in most cases, the inner deV component is well resolved. The double-component ETGs that we probe in this work are those showing changes in isophotal shape on kpc scales, beyond the central part of the galaxy that may be most affected by any uncertainties in the PSF.

4. RESULTS

4.1. General characteristics

Of the 838 elliptical galaxies in our sample, we find 388 double component ETGs (46%), 220 with high confidence (HC; 26% of the total). This number alone is interesting; a significant fraction of nearby elliptical galaxies have complex photometric substructures that cannot be well described by a single Sérsic model.

We first present the general characteristics of the subcomponents of our double component ETGs. For consistency, we measure all sizes in the same manner. When referring to the size of a galaxy, we use the single Sérsic fit, which in general provides the best overall fit to the light profile. We will also consider the size (effective semi-major axis) of each subcomponent for double component ETGs.

Figure 8 shows the density histograms of the size and ellipticity of the best-fit models for single and double component ETGs. We first compare the sizes measured from a single Sérsic model for the single and double component ETGs (black dashed and solid lines), and we do not find any significant difference between the two groups. For double component ETGs, we also examine the component size and ellipticity for the deV (red) and Exp (blue) components. The inner deV and outer Exp

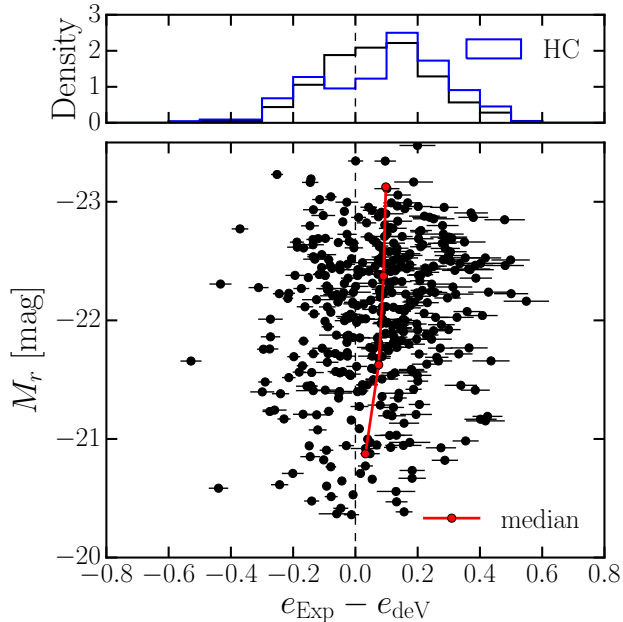


FIG. 9.— Difference in ellipticity of subcomponents vs. r -band absolute magnitude. The red circle connects the median in different magnitude bins. In the upper panel, we show the density histogram of the difference in ellipticities for double component ETGs, and highlight double component with high confidence with blue.

component have characteristic sizes of 2.3 – 4.6 kpc and 9.2 – 20.5 kpc, respectively (25 – 75 percentile). Since our selection of double component ETGs is based on the radial change in ellipticity, the change in isophotal shape is occurring between these two characteristic radii.

We also compare the ellipticity of the two components in Figure 8. Since the shape of the deV is essentially the same as that measured using the single Sérsic model (Figure 6), we see no difference in the central ellipticity for the single and double component ETGs. In the double component ETGs, the outer Exp components are found to extend to higher ellipticity than the deV components. The median ellipticity for the deV and Exp components are 0.22 and 0.29, with standard deviation of 0.12 and 0.15, respectively. Figure 9 shows the distribution of the difference in ellipticity between the deV and Exp component of the deVExp model. On average, the outer component is more flattened than the inner component with median $\Delta e \approx 0.082$. This difference is more pronounced when considering only the double component HC ETGs (median $\Delta e \approx 0.12$). The large scatter in ellipticity change argues for a stochastic nature to the buildup of the outer component.

Our results are both qualitatively and quantitatively similar to the findings of Huang et al. (2013b), despite the differences in modeling approach. The outer component in their three component models, with a median effective radius of ≈ 10 kpc, is similar in scale to the Exp component of our model. Their largest component also tends to show higher ellipticities compared to the inner and middle at the level of $\Delta e \lesssim 0.1$. They additionally find that the skewness towards more elliptical profiles is most pronounced in the high luminosity subsample ($M_V \leq -21.3$ mag). We note that there is a weak trend of increasing ellipticity difference with increasing

luminosity within our double component ETGs as well (Figure 9; Pearson $r = -0.15$ with magnitude). Considering that we intentionally selected ETGs that show significant change in ellipticity, we also checked for a correlation between the fraction of double component ETGs and the r -band magnitude, but do not find such a correlation.

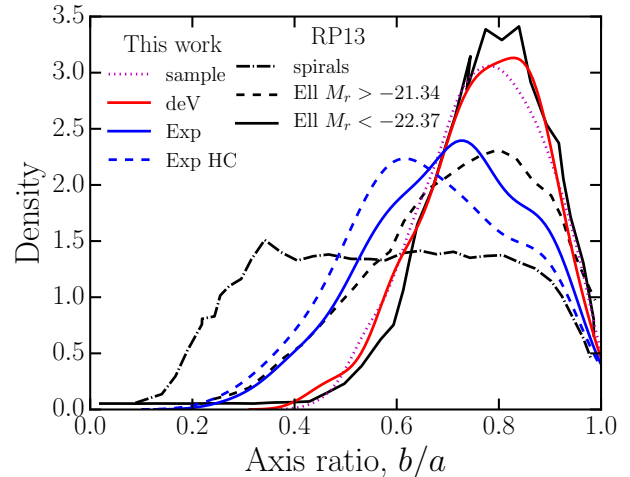


FIG. 10.— Axis ratio distribution of the sample and the double component ETGs. The axis ratio distribution for the entire sample from the single Sérsic model (dotted magenta) and the axis ratios of each subcomponent, deV (red) and Exp (blue) of the double component ETGs are presented. We highlight the distribution for the Exp component of the double component ETGs with high confidence with blue dashed line. For comparison, we show the distribution for the highest and lowest luminosity bins of ellipticals, and for the spirals from Rodríguez & Padilla (2013). Density distributions are obtained from kernel density estimation using a Gaussian kernel. We find that the Exp component in the double component ETGs are more flattened than ellipticals, but their ellipticity distribution is still different from that of spiral galaxies, arguing that the outer components are not as flattened as exponential disks.

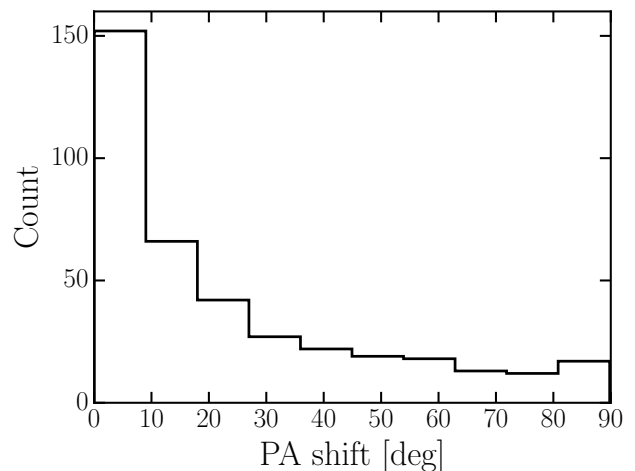


FIG. 11.— Histogram of the PA shift between the deV and Exp component of the deVExp model for double component ETGs.

The distribution in ellipticity for ensembles of stellar systems can provide valuable clues to their intrinsic shape, which is ultimately connected to the formation history (Tremblay & Merritt 1996). We compare the

axis ratio distribution of our double component ETGs with the latest morphology-specific galaxy axis ratio distribution from Rodríguez & Padilla (2013). Their study models the axis ratio distribution of SDSS galaxies as the random projection of a triaxial spheroid characterized by ellipticity $\epsilon = 1 - B/A$ and thickness $\gamma = C/A$, where A , B , C are the major, middle, and minor axes. Elliptical galaxies show a variation in the apparent ellipticity distribution with increasing absolute magnitude in the sense that more luminous galaxies tend to be rounder (Rodríguez & Padilla 2013). The variation is driven mainly by the thickness (γ) that ranges from 0.584 for the least luminous to 0.655 for the most luminous group, while the ellipticity is always quite small (≈ 0.1). Figure 10 compares the axis ratio distribution of each subcomponent of the double component ETGs with the least and most luminous ellipticals from Rodríguez & Padilla (2013). First, we find the overall distribution of axis ratios of the entire sample to be consistent with Rodríguez & Padilla (2013) given that more than half of the galaxies in our sample have an r -band magnitude brighter than -21.9 mag (em3 and em4 in their paper). For double component ETGs only, we compare the distribution of each subcomponent to these references. While the distribution of the inner deV component is very similar to that of the entire sample and the most luminous ellipticals, the Exp component shows a broader distribution, implying more flattened systems. In fact, compared to the least luminous ellipticals from Rodríguez & Padilla (2013) with $\langle \gamma \rangle = 0.543$ and $\langle \epsilon \rangle = 0.122$, there is an indication that the Exp component probed in this study would be even more flattened. However, we note that the distribution is still distinctively different from spiral galaxies (dash-dotted line), from which we infer that we are not simply identifying S0s.

We briefly compare our results with the two component decomposition of Meert et al. (2015). Of 682 galaxies that are common in both studies, we find that the number of two-component galaxies using the same model (deVExp) of Meert et al. (2015) is 399 (59%). This higher fraction is probably due to the less restrictive criteria of Meert et al. (2015), which does not explicitly utilize ellipticity profiles. The membership of two component galaxy also differs in detail: 249 out of 399 two component galaxies are also double component ETGs in our study while 57 of the double component ETGs in this study are not labeled two-component by Meert et al. (2015). The general characteristics of size and ellipticity of their deVExp model are in good agreement with our results. In their fits, the deV and Exp components have typical sizes of 2.4 – 5 kpc and 7 – 17 kpc respectively (25 – 75 percentiles), comparable to our values. They also find that the ellipticity distribution of Exp component is more flattened than deV component, yet is not as flattened as rotational disks.

We address the possibility that the observed change in shape in the ETGs may actually be an isophotal twist in a single triaxial component. The distribution of PA shifts between the two components is shown in Figure 11. Only 25% of the double component ETGs show a PA shift larger than 38 degrees between the two components, and almost half of the double component ETGs are aligned within 10 degrees. As it is unlikely that the line of sight is along the axis of a triaxial body in such large frac-

tion of random projections, triaxiality, although it may be of some importance, cannot fully account for ellipticity changes (Gonzalez et al. 2005). Another telltale sign of triaxiality is a misalignment between the photometric and kinematic major axes. Krajnović et al. (2011) investigated the distribution of this misalignment for ATLAS^{3D} ETGs and found that most (90 %) of the ETGs aligned within 15 degrees, consistent with axisymmetry within one R_e .

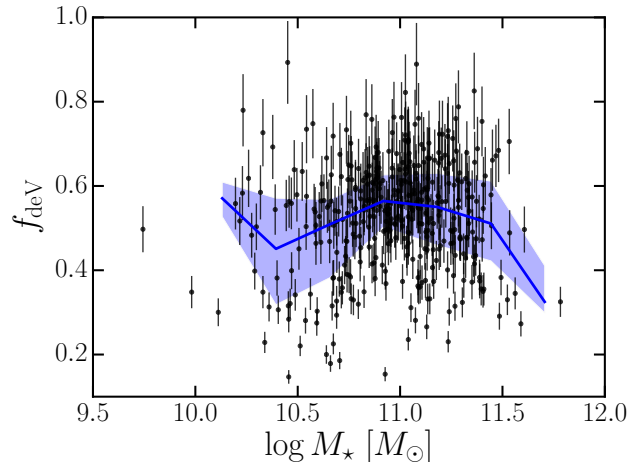


FIG. 12.— Flux fraction of inner deV component as a function of total stellar mass. We show the median and 25 – 75 percentiles in equally spaced $\log M_*$ bins from 10 to 12 with the blue solid line and shaded regions.

We examine the flux fraction of the inner deV component in Figure 12. We use the single Sérsic model to estimate the total flux, as the deVExp model misses some of the flux from the outermost part (section 3). The fraction of flux in the deV component f_{deV} shows a quite broad distribution spanning ~ 0.2 to 0.8 and typically is around 0.6 . This, in turn, means that the fraction of light from the outer parts, which is possibly material that is accreted after the core forms, shows a large range. The flux fraction only shows a weakly increasing trend with the total stellar mass (pearson $r = 0.11$ for the whole sample). A similar level of stochasticity is observed for the outer components of the Huang et al. (2013b) decompositions (their figure 29) for ETGs more massive than $\log M_* > 10^{10.5} M_\odot$.

Elliptical galaxies show tight correlations between size, luminosity, and σ , known as the fundamental plane (FP; Dressler et al. 1987; Djorgovski & Davis 1987; Bernardi et al. 2003; Saulder et al. 2013). We may ask whether the deV components of the double-component ETGs follow the same scaling relations. We take the FP coefficients from Saulder et al. (2013) for the SDSS r -band. This relation was derived for ETGs using the circularized radius $R_0 = R_e \sqrt{1 - e}$ and the effective surface brightness I_e from a single de Vaucouleurs model fit. We first check for consistency using the same model for the entire sample in Figure 13 (black points), and find that the agreement is good. For double component ETGs, we find that the inner deV component essentially moves parallel to the original FP with similar scatter. The apparent deviation from the FP at small sizes ($R_0 < 1$ kpc) for the

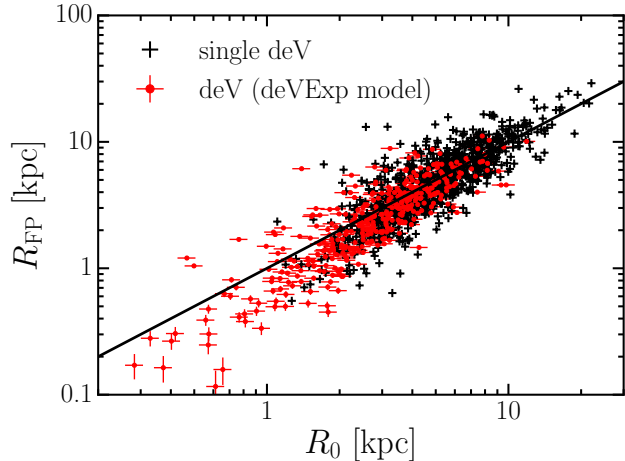


FIG. 13.— Distribution of the inner deV component of the best-fit deVExp models for double component ETGs on the fundamental plane (FP) defined by Saulder et al. (2013). We first check that the traditional single deV model parameters for our sample (black crosses) are consistent with their FP (black line). The inner deV component for double component ETGs (red circles) is shifted to smaller sizes, but moves along the FP.

inner deV components mostly correspond to marginally resolved cases with sizes comparable to the PSF (see section 3.3).

4.2. Correlations

To shed more light on the nature of the double component ETGs, we explore correlations between the frequency of double component ETGs and the intrinsic or environmental parameters of each galaxy. Figure 14 shows the distribution of key intrinsic parameters for single and double component ETGs. In each bin, we calculate the fraction of double component (HC) ETGs, which are connected at the bin center by solid (dashed) lines. By far the strongest trend we find is that high Sérsic index (n) ETGs are more likely to be double component (Figure 14a). Considering that the Sérsic functions tend to be more centrally concentrated and more extended at fixed surface brightness as n increases, this trend may seem trivial; a deVExp model will naturally work better when a galaxy has a more extended outer surface brightness profile and thus high n . However, the important thing to note is that our selection for double component ETGs is based on the ellipticity profile, or isophotal shape. Thus, we find that ETGs with high Sérsic index are also more likely to show a radial change in ellipticity that is better modeled by using a two component model.

It is possible that some of the low Sérsic n galaxies also contain a change in isophote shape, yet were mislabeled as single component because we fix the inner index to $n = 4$ and fail to find a good model that simultaneously fits the overall radial profile and the shape. As a test, we fitted a double Sérsic model with both indices free (between 0.1 and 9) to test whether our choice of indices were reasonable, and whether our selection of double component ETGs changes significantly. We find that although there is a significant spread in indices of both the inner and outer component, they range from $n \sim 3$ to ~ 6 and $n < 1$ to ~ 2 for the inner and outer component, respectively, not far from our choice of $n = 4$ and $n = 1$.

Since the double component ETGs in this work are selected based on their ellipticity distribution, we do not expect our selection of double component ETGs to be significantly altered. The component ellipticities of the double Sérsic model match our default deVExp model with a scatter of ~ 0.1 . One should also keep in mind that the Sérsic n depends sensitively on how many Sérsic components are fitted. For example, in the three component model of Huang et al. (2013b), most of the components have $n \lesssim 3$.

We also find an increasing fraction of double component ETGs with increasing velocity dispersion [Panel (b) of Figure 14]. This correlation is not independent of the correlation with Sérsic index, as the velocity dispersion correlates with Sérsic n (Pearson $r = 0.31$ for the whole sample). No similar trend is found with stellar mass [Panel (c)]. This may be related to the fact that velocity dispersion is a better tracer of the central potential and the stellar population of ETGs in general than the stellar mass (Bender et al. 1993; Trager et al. 2000; Graves et al. 2009a; Wake et al. 2012; Greene et al. 2015).

Figure 15 shows the fraction of double component ETGs as a function of projected neighbor density from Baldry et al. (2006). The projected neighbor density is defined by averaging the surface density of galaxies within the distance to the 4th or 5th nearest neighbor to a galaxy. Since the fraction correlates with the velocity dispersion σ , we divide the sample into different σ bins (colored lines), and also show all σ combined (black dashed line). The error bars reflect the 25th and 75th percentile of the fractional distribution after bootstrapping the sample 1000 times, assuming that our selection of double component ETGs is correct. We find that the fraction of double component ETGs decreases significantly with increasing Σ at $\log \Sigma \gtrsim -0.5$, except for the highest σ bin.

4.3. Stellar Populations

In this section, we use the SDSS spectra to look at the stellar population properties of the single and HC double component galaxies. Since it is well-known that the stellar population properties of ETGs are a strong function of central stellar velocity dispersion (e.g., Trager et al. 2000; Graves et al. 2009a; van Dokkum et al. 2014) we stack as a function of stellar velocity dispersion for both the single-component and high-confidence double-component galaxies. We also stack as a function of stellar mass. We have no fewer than 15 galaxies per stack. Note that, given the size of the SDSS spectroscopic fibers (3 arcsec), we probe the central stellar population such that light from the outer component of the two-component ETGs does not contribute to the light in the fiber.

Our procedure is as follows. First, we jointly fit the stellar continuum and strong emission lines using pPXF+Gandalf (Cappellari & Emsellem 2004; Sarzi et al. 2006). We subtract emission before stacking, but to be conservative we also remove the galaxies with H α emission line EW $> 0.5 \text{ \AA}$, comprising $< 10\%$ of all galaxies.

We then follow the stacking procedure described in detail in Greene et al. (2013, 2015). We divide each spectrum by a heavily smoothed version of itself to remove the continuum and then combine the spectra using the biweight estimator (Beers et al. 1990). We measure Lick

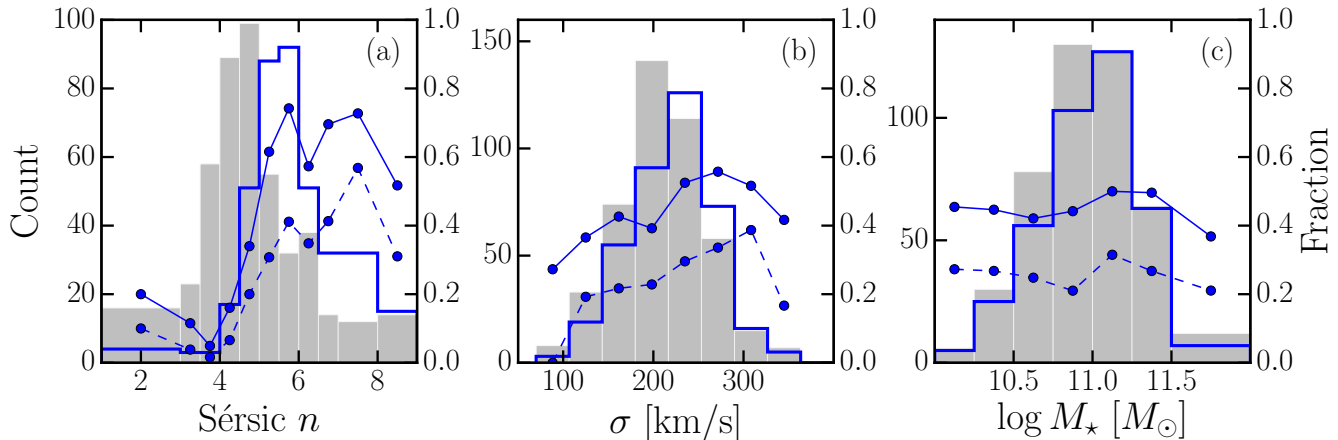


FIG. 14.— Histogram of galaxy parameters for single (gray bars) and double (blue steps) component ETGs. Solid (dashed) lines show the fraction of double component (HC) ETGs in each bin, with values on the right y-axis. The parameters are (a) Sérsic index n from the best-fit single Sérsic model, (b) galaxy velocity dispersion, and (c) photometric stellar mass.

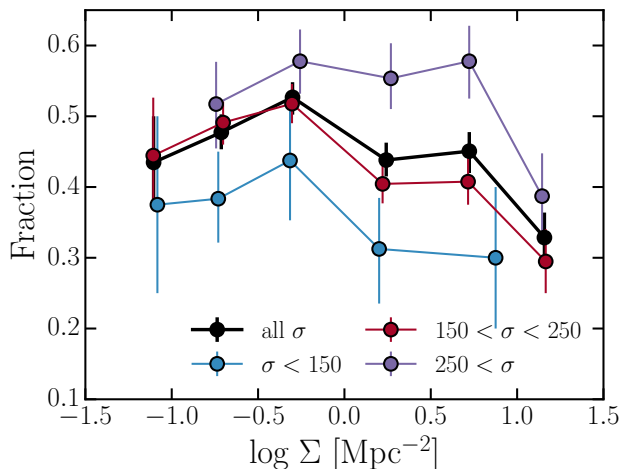


FIG. 15.— Fraction of double component ETGs as a function of projected neighbor density (Baldry et al. 2006). We show the trend in bins of σ . There is a weak trend towards a decreasing double component fraction with increasing galaxy densities.

indices from each stack and use the code EZ_Ages to invert the measured indices and infer luminosity-weighted mean stellar ages, $[\text{Fe}/\text{H}]$, and $[\alpha/\text{Fe}]$ (for details see Graves & Schiavon 2008). We derive errors through a bootstrapping procedure in which we generate 200 mock stacks drawing the same number of galaxies from the full list with replacement.

The result is shown in Figure 16. We compare the luminosity-weighted age, $[\text{Fe}/\text{H}]$, and $[\alpha/\text{Fe}]$ as a function of σ for single (black) and double (red) component ETGs. The median, 70%, and 95% of the distribution from the bootstrapping is indicated with circles, darker, and lighter shaded regions respectively. While we find no difference at low $\sigma < 200 \text{ km s}^{-1}$, at higher dispersion the double component ETGs tend to be younger and more metal-rich. Although the difference in α -enhancement is insignificant in most bins, there is a hint at the highest σ bin that the double component ETGs may be less α -enhanced. We find no such trends in stellar populations when the spectra are binned in stellar mass, although the range of stellar mass explored is narrow.

To test the importance of emission line subtraction, we

perform our analysis with no subtraction at all (clearly unrealistic). While the ages move systematically by ~ 2 Gyr, the difference in age between the two populations is preserved.

4.4. Mass-Size Relations

In this section, we explore the mass-size relation of our sample relative to literature that looks at the evolution of the relation from $z = 3$ to the present. For comparison, we take the observed mass-size relations for quiescent samples from van der Wel et al. (2014) between their highest ($z = 2.75$) and lowest ($z = 0.25$) redshift bins to summarize the evolution in the mass-size relation from $z = 3$ to the present. Their sizes are measured by modeling *HST* images with a single Sérsic function (van der Wel et al. 2012), and converted to size at the wavelength of 5000 \AA .

We first compare the equivalent single Sérsic model sizes from our sample with the $z = 0.25$ distribution, shown in the left panel of Figure 17. As discussed previously in §4.1 and 4.2, the single and double component galaxies have similar size and mass distributions, and the loci of the two groups coincide in the mass-size plane. This also provides a consistency check. As expected, the loci of our single-component fits lie slightly above those of the $z = 0.25$ galaxies (lookback time ≈ 3 Gyr). For comparison with van der Wel, we perform a power-law fit to the single Sérsic sizes for galaxies with $M_* > 2 \times 10^{10} M_\odot$ (consistent with van der Wel et al. 2014) with a random error of 20% in R_e and 0.1 dex in $\log M_*$ (Kannappan & Gawiser 2007). We fit for A , and α in $R_e/\text{kpc} = A(M_*/5 \times 10^{10} M_\odot)^\alpha$. The best-fit values of $\log A$ and α are 0.73 ± 0.02 and 0.70 ± 0.05 . We find that the relation for our sample at the median redshift of 0.043 is consistent with that of the quiescent galaxies at $z = 0.25$ in van der Wel et al. (2014) with a slight offset towards larger sizes.

For double component ETGs, we compare the mass-size relation for each subcomponent on the right panel of Figure 17. We assign to each component a fraction of the total stellar mass proportional to its flux. Similarly, a power-law fit to the deV component yields $\log A$ and α of 0.50 ± 0.02 and 0.74 ± 0.09 . While the slope remains unchanged within errors, the mass-size relation for the deV

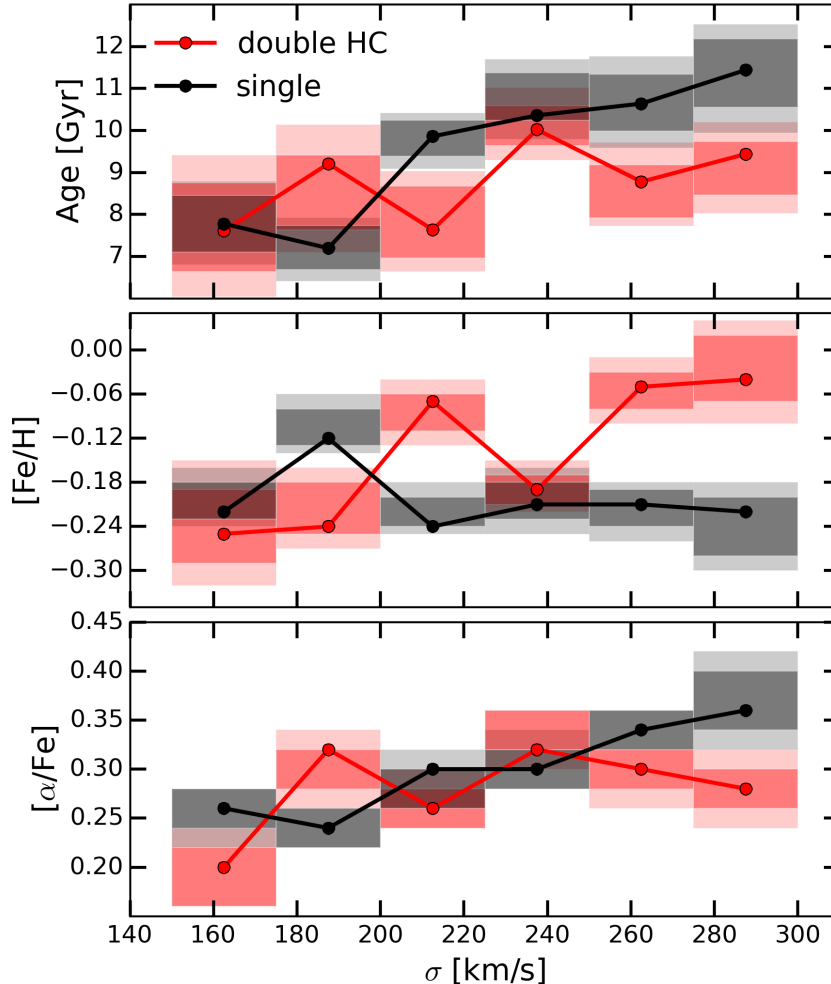


FIG. 16.— Stellar population difference between single and HC double component ETGs. Lines, dark and light shaded regions correspond to median, 70 and 90 percentiles around median respectively from bootstrapping. The bins in σ are chosen such that we have no fewer than 15 galaxies per bin. At $\sigma > 200 \text{ km s}^{-1}$ we find that the double component (HC) galaxies tend to be younger and more metal-rich.

component falls in between the relations at $z = 0.75$ and $z = 0.25$ presented in van der Wel et al. (2014). The size measurements of van der Wel et al. (2014) are corrected to be at the rest-frame wavelength $\lambda = 5000 \text{ \AA}$. Although we do not correct our effective radii, they are measured in the SDSS r -band images ($\lambda = 6231 \text{ \AA}$), so the $\approx 5\%$ correction cannot explain the offset in the mass-size relation. Thus, it is plausible that the inner deV component in double component ETGs may be the relic of the smaller, quiescent galaxies at $z \sim 0.5$ while the outer Exp component assembled later, shifting the overall mass-size relation towards the present-day relation.

5. DISCUSSION & SUMMARY

In this study, we have performed a double component model fitting to a sample of morphological elliptical galaxies in the nearby universe. We have argued that the primary reason for preferring a double component model to a single Sérsic model is the radially changing shapes (ellipticities) of the isophotes, and selected “double component” ETGs based on whether the double component model provides a better fit to the ellipticity profile. We

now examine whether and how the results presented in the previous sections may be tied together in a consistent scenario of the evolution of elliptical galaxies, in association with the recent studies on ETGs.

First, we summarize the key findings of this paper as follows:

- We find that a significant fraction (46 %) of the nearby ETGs in our sample require multiple photometric components to describe their radial changes in isophotal shape. By fitting a two-component model to the surface brightness, we obtain that the characteristic sizes of the inner deV and outer Exp component are $\sim 3 \text{ kpc}$ and $\sim 20 \text{ kpc}$ respectively. The outer component tends to be more flattened than the inner, and this trend gets stronger with increasing luminosity.
- However, at the same time, both the shape and the flux fraction of the Exp component show significant spread at fixed stellar mass or luminosity. Interestingly, the inner component of the double-component galaxies follow the same fundamental

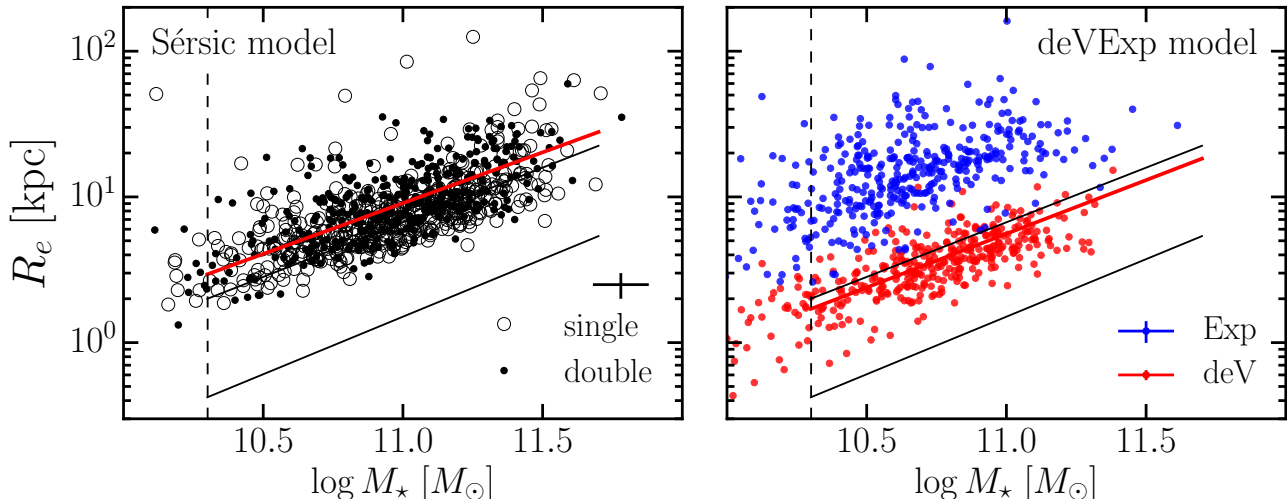


FIG. 17.— Mass-size relations of single and double component ETGs. On the left, we show the single Sérsic model sizes for the single and double component galaxies. We find that the double component ETGs do not separate from the single component ETGs on the mass-size plane. A power-law fit to the galaxies with $M_\star > 2 \times 10^{10} M_\odot$ (vertical dashed line) is shown in the red line. On the right, we show the mass-size relation for each component of the deVExp model for double component ETGs. Similarly, we show a power-law fit to the deV component in red. In each panel, the upper and lower black lines show the mass-size relations from van der Wel et al. (2014) at the lowest and highest redshift bins ($z = 0.25$ and $z = 2.75$), which encloses the entire range from the present day to $z = 3$. The typical errors in x and y are indicated in the lower left.

plane relation derived from fitting a single component model for all ETGs, with similar scatter.

- Centrally concentrated (high Sérsic index), high σ ETGs are more likely to require a two-component fit to explain their isophotal shape. The fraction of ETGs classified as double component shows a decreasing trend with the surface neighbor density at $\log \Sigma \gtrsim -0.5 \text{ Mpc}^{-2}$ except for the highest σ ETGs ($\sigma > 250 \text{ km s}^{-1}$).
- The stellar populations of single and double component ETGs are different. The double component ETGs generally tend to be younger and more metal-rich at $\sigma > 200 \text{ km s}^{-1}$.
- The mass-size relation of the inner deV component in double component ETGs falls between the relation of quiescent galaxies at $z = 0.25$ and $z = 0.75$ (van der Wel et al. 2014) suggesting that the inner cores may have been in place at $z=0.75$ and the outer components assembled later.

The results of this study are in general agreement with the recent multi-component fitting analysis of Huang et al. (2013b) as discussed in section 4. Because of the difference in image quality, we do not resolve the inner component seen in their work with median $R_e < 1 \text{ kpc}$, and the inner and middle component of their decomposition would likely be jointly described by the deV in our deVExp model.

Both our work and Huang et al. (2013b) find that the outer parts of nearby ETGs tend to be more elliptical than the central component, and that this trend correlates with luminosity. It is interesting to note that the even fainter and more extended stellar halos of high concentration, massive galaxies seem to continue this trend, showing higher ellipticity with increasing stellar mass (D’Souza et al. 2014). As opposed to Huang et al.

(2013a), who found that multi-component fits are preferred in more than 75% of the local ETGs in their sample, we find a smaller fraction of galaxies require two components, and we uncover other interesting physical differences between the two samples. Our selection and the fraction of double component ETGs in this work is more conservative in the sense that we require a threshold change of χ_e^2 as well as a condition for the second component to dominate the surface brightness at some region.

The inner deV component of our model with a typical $R_e \sim 3 \text{ kpc}$ moves along the fundamental plane and shows a tight mass-size relation (Figure 13, 17). On the other hand, the nature of the outer Exp components seem to be more stochastic. They contribute a wide range in total galaxy light ($\sim 0.3 - 0.8$) without any correlation with the total stellar mass (Figure 12). Even though their shapes tend to more elliptical with increasing luminosity, the dispersion is still quite large (Figure 9).

The structures of ETGs are known to show connections with their central stellar population (e.g., Forbes et al. 1998; Terlevich & Forbes 2002; Graves et al. 2009b). The age, metallicity and abundances of ETGs strongly correlate with σ but not with size (R_e). We also find that the fraction of double component ETGs showing kpc-scale changes in isophote shape increases with σ but is independent of the overall size typically measured by single component fitting. Moreover these studies suggest that the scatter about the fundamental plane may correlate with age such that at fixed σ and size, galaxies with higher mean effective surface brightness are younger, more Fe-rich, and have lower $[\text{Mg}/\text{Fe}]$ than the counterparts with lower mean surface brightness (Graves & Faber 2010; Graves et al. 2010). Our double component ETGs are analogous to the high surface brightness galaxies in the Graves et al. work, since the high n values at fixed σ that characterize these galaxies translates directly into higher surface brightness at fixed size. Likewise, the

double component galaxies show younger ages and are more Fe-rich. What is new here is that we link high central surface brightness with a more prominent flattened outer component

We suggest as a possible scenario that the double component ETGs are relics of relatively recent ($z \lesssim 1$) mass accretion onto the outskirts of compact cores, whereas single component ETGs completed this process earlier. This is supported by the younger age and under-dense environment for double component ETGs relative to the single. Older galaxies in denser environment may have experienced a similar mass accretion process at earlier times, but the signature of such events probed in this work by radially changing ellipticity may be washed out with time, leading us to classify them as single component ETGs. Ongoing minor mergers in the double-component galaxies may drive the Sérsic index to a higher value by adding mass at large radius (Hilz et al. 2013).

From the perspective of the evolution of compact high- z systems, the double component ETGs may be those where the early core survives relatively intact. Wellons et al. (2016) studied 35 massive, compact galaxies at $z \approx 2$ in the Illustris simulation (Vogelsberger et al. 2014; Genel et al. 2014), a suite of cosmological hydrodynamic simulations including baryonic physics and sampling a large number of massive galaxies ($M_* = 10^9 - 10^{12} M_\odot$), and suggest that the evolutionary paths of these systems are varied. The most common outcome, occurring for roughly half of the sample, is that a compact, massive galaxy survives as the core of a more massive galaxy at $z = 0$, with the outer envelope from merger and accretion. This is roughly consistent with our findings. On the other hand, in the simulation the compact cores at $z = 2$ in denser environment are more likely to gain stellar mass at larger radii (but also see Damjanov et al. 2015). If all of the mass accumulation at large radius is detectable in our study as changes in ellipticity profile, then the simulation results differ from our finding that the fraction of double component ETGs decrease in denser environment. Thus far, there are no predictions on differences in the stellar population for the different outcomes.

Recently, Rodriguez-Gomez et al. (2016) also looked at the in-situ mass fraction of massive galaxies in the same simulation. They found that at fixed stellar mass, galaxies hosted by halos with later formation times also have a higher mass fraction in ex-situ stars than their early-formed counterparts. While in their simulation they did not see a dependence on the mass-weighted stellar age, it is still interesting to consider the possibility that we have found a sub-population of galaxies with the highest ex-situ fraction, and that this fraction appears to be linked with central stellar-population age.

Given that the double component ETGs have younger central stellar population age, it is also possible that these galaxies joined the red sequence more recently, and their outer components of higher ellipticities are from

their dissipational past rather than from size growth of the inner component (cores). This would not necessarily support progenitor bias as the distribution of the single-component model sizes of the two groups are similar.

The presence of extended light in galaxy outskirts has long been known to exist ubiquitously for the brightest cluster galaxies (BCGs) (e.g., Oemler 1976; Schombert 1988; Gonzalez et al. 2005). This “cD envelope” is thought to have assembled from the tidal interaction of cluster galaxies (Murante et al. 2004; Willman et al. 2004; Sommer-Larsen et al. 2005; Martel et al. 2012; Cooper et al. 2015) that forms intracluster light that traces the potential of the cluster. A tantalizing similarity between the excess light around BCGs and massive ETGs is that they are both largely aligned with the “core” component, and more flattened (Porter et al. 1991; Gonzalez et al. 2005; Zibetti et al. 2005). Furthermore, in the case of BCGs, the orientation of the cluster galaxy distribution is aligned with the BCGs (e.g., Binggeli 1982). Taken together, the elongation of the cD envelope may be an imprint of the disruption of galaxies falling into the cluster on primarily radial orbits (Moore et al. 1996). This effect will be more pronounced at large radial distances as the dynamical time is longer. Although on a different scale, we suspect a similar process might explain the elliptical outskirts that we measure here around individual galaxies.

In this work, we modelled the surface brightness of nearby ETGs with a multi-component model to argue that the large-scale radial changes in ellipticity of many ETGs require a multi-component model to fully capture its morphology. We showed that this property may correlate with the properties of the central stellar population, further hinting at the physical significance of such decomposition. In recent years, there have been significant efforts to connect the kinematics of the central region of ETGs to their cosmological evolution (e.g., Naab et al. 2014). From the kinematics within $\lesssim 1R_e$, ETGs are commonly classified as either slow or fast rotators (Emsellem et al. 2007, 2011). The connection between such classification, and our selection of double component ETGs is yet unclear. Upcoming IFU surveys such as MANGA (Bundy et al. 2015) will be able to study the connections between morphology, kinematics, and stellar population of ETGs in greater detail, and ultimately how they are tied to the formation history.

We thank Song Huang, Chung-Pei Ma and Kevin Bundy for useful discussions. We also thank the referee for his/her detailed comments and suggestions that significantly improved the paper. SO thanks Peter Erwin for his help with using IMFIT. This research made use of Astropy, a community-developed core Python package for Astronomy (Astropy Collaboration, 2013), and matplotlib (Hunter 2007). JEG is partially supported by NSF grant AST-1411642.

REFERENCES

- Akaike, H. 1974, IEEE Transactions on Automatic Control, 19, 716
 Baldry, I. K., Balogh, M. L., Bower, R. G., et al. 2006, MNRAS, 373, 469
 Beers, T. C., Flynn, K., & Gebhardt, K. 1990, AJ, 100, 32
 Bell, E. F., van der Wel, A., Papovich, C., et al. 2012, ApJ, 753, 167
 Bender, R., Burstein, D., & Faber, S. M. 1993, ApJ, 411, 153

- Bernardi, M., Sheth, R. K., Annis, J., et al. 2003, *AJ*, 125, 1866
- Binggeli, B. 1982, *A&A*, 107, 338
- Blanton, M. R., Kazin, E., Muna, D., Weaver, B. A., & Price-Whelan, A. 2011, *AJ*, 142, 31
- Blanton, M. R., Schlegel, D. J., Strauss, M. A., et al. 2005, *AJ*, 129, 2562
- Boylan-Kolchin, M., Ma, C.-P., & Quataert, E. 2006, *MNRAS*, 369, 1081
- Brinchmann, J., Charlot, S., White, S. D. M., et al. 2004, *MNRAS*, 351, 1151
- Buitrago, F., Trujillo, I., Conselice, C. J., et al. 2008, *ApJ*, 687, L61
- Bundy, K., Bershad, M. A., Law, D. R., et al. 2015, *ApJ*, 798, 7
- Caon, N., Capaccioli, M., & D’Onofrio, M. 1993, *MNRAS*, 265, 1013
- Cappellari, M., & Emsellem, E. 2004, *PASP*, 116, 138
- Carollo, C. M., Bschorr, T. J., Renzini, A., et al. 2013, *ApJ*, 773, 112
- Cassata, P., Giavalisco, M., Williams, C. C., et al. 2013, *ApJ*, 775, 106
- Cooper, A. P., Gao, L., Guo, Q., et al. 2015, *MNRAS*, 451, 2703
- Daddi, E., Renzini, A., Pirzkal, N., et al. 2005, *ApJ*, 626, 680
- Damjanov, I., Hwang, H. S., Geller, M. J., & Chilingarian, I. 2014, *ApJ*, 793, 39
- Damjanov, I., Zahid, H. J., Geller, M. J., & Hwang, H. S. 2015, *ApJ*, 815, 104
- Damjanov, I., Abraham, R. G., Glazebrook, K., et al. 2011, *ApJ*, 739, L44
- Djorgovski, S., & Davis, M. 1987, *ApJ*, 313, 59
- Dressler, A., Lynden-Bell, D., Burstein, D., et al. 1987, *ApJ*, 313, 42
- D’Souza, R., Kauffman, G., Wang, J., & Vegetti, S. 2014, *MNRAS*, 443, 1433
- Emsellem, E., Cappellari, M., Krajnović, D., et al. 2007, *MNRAS*, 379, 401
- , 2011, *MNRAS*, 414, 888
- Erwin, P. 2015, *ApJ*, 799, 226
- Fan, L., Lapi, A., De Zotti, G., & Danese, L. 2008, *ApJ*, 689, L101
- Forbes, D. A., Ponman, T. J., & Brown, R. J. N. 1998, *ApJ*, 508, L43
- Genel, S., Vogelsberger, M., Springel, V., et al. 2014, *MNRAS*, 445, 175
- Gonzalez, A. H., Zabludoff, A. I., & Zaritsky, D. 2005, *ApJ*, 618, 195
- Graham, A. W., & Driver, S. P. 2005, *PASA*, 22, 118
- Graham, A. W., Dullo, B. T., & Savorgnan, G. A. D. 2015, *ApJ*, 804, 32
- Graves, G. J., & Faber, S. M. 2010, *ApJ*, 717, 803
- Graves, G. J., Faber, S. M., & Schiavon, R. P. 2009a, *ApJ*, 693, 486
- , 2009b, *ApJ*, 698, 1590
- , 2010, *ApJ*, 721, 278
- Graves, G. J., & Schiavon, R. P. 2008, *ApJS*, 177, 446
- Greene, J. E., Janish, R., Ma, C.-P., et al. 2015, *ApJ*, 807, 11
- Greene, J. E., Murphy, J. D., Graves, G. J., et al. 2013, *ApJ*, 776, 64
- Hilz, M., Naab, T., & Ostriker, J. P. 2013, *MNRAS*, 429, 2924
- Hopkins, P. F., Bundy, K., Hernquist, L., Wuyts, S., & Cox, T. J. 2010, *MNRAS*, 401, 1099
- Hopkins, P. F., Lauer, T. R., Cox, T. J., Hernquist, L., & Kormendy, J. 2009, *ApJS*, 181, 486
- Huang, S., Ho, L. C., Peng, C. Y., Li, Z.-Y., & Barth, A. J. 2013a, *ApJ*, 768, L28
- , 2013b, *ApJ*, 766, 47
- Hunter, J. D. 2007, *Computing In Science & Engineering*, 9, 90
- Jeffreys, H. 1961, *Theory of Probability*, 3rd edn. (Oxford, England: Oxford)
- Kannappan, S. J., & Gawiser, E. 2007, *ApJ*, 657, L5
- Kauffmann, G., Heckman, T. M., White, S. D. M., et al. 2003a, *MNRAS*, 341, 33
- Kauffmann, G., Heckman, T. M., Tremonti, C., et al. 2003b, *MNRAS*, 346, 1055
- Keating, S. K., Abraham, R. G., Schiavon, R., et al. 2015, *ApJ*, 798, 26
- Kewley, L. J., Dopita, M. A., Sutherland, R. S., Heisler, C. A., & Trevena, J. 2001, *ApJ*, 556, 121
- Kormendy, J., Fisher, D. B., Cornell, M. E., & Bender, R. 2009, *ApJS*, 182, 216
- Krajnović, D., Emsellem, E., Cappellari, M., et al. 2011, *MNRAS*, 414, 2923
- Lackner, C. N., & Gunn, J. E. 2012, *MNRAS*, 421, 2277
- Martel, H., Barai, P., & Brito, W. 2012, *ApJ*, 757, 48
- McGrath, E. J., Stockton, A., Canalizo, G., Iye, M., & Maihara, T. 2008, *ApJ*, 682, 303
- Meert, A., Vikram, V., & Bernardi, M. 2013, *MNRAS*, 433, 1344
- , 2015, *MNRAS*, 446, 3943
- Moore, B., Katz, N., Lake, G., Dressler, A., & Oemler, A. 1996, *Nature*, 379, 613
- Moresco, M., Pozzetti, L., Cimatti, A., et al. 2013, *A&A*, 558, A61
- Murante, G., Arnaboldi, M., Gerhard, O., et al. 2004, *ApJ*, 607, L83
- Naab, T., Johansson, P. H., & Ostriker, J. P. 2009, *ApJ*, 699, L178
- Naab, T., Oser, L., Emsellem, E., et al. 2014, *MNRAS*, 444, 3357
- Nair, P. B., & Abraham, R. G. 2010, *ApJS*, 186, 427
- Newman, A. B., Ellis, R. S., Bundy, K., & Treu, T. 2012, *ApJ*, 746, 162
- Oemler, Jr., A. 1976, *ApJ*, 209, 693
- Oser, L., Ostriker, J. P., Naab, T., Johansson, P. H., & Burkert, A. 2010, *ApJ*, 725, 2312
- Poggianti, B. M., Moretti, A., Calvi, R., et al. 2013, *ApJ*, 777, 125
- Porter, A. C., Schneider, D. P., & Hoessel, J. G. 1991, *AJ*, 101, 1561
- Rodríguez, S., & Padilla, N. D. 2013, *MNRAS*, 434, 2153
- Rodríguez-Gomez, V., Pillepich, A., Sales, L. V., et al. 2016, *MNRAS*, 458, 2371
- Sarzi, M., Falcón-Barroso, J., Davies, R. L., et al. 2006, *MNRAS*, 366, 1151
- Saulder, C., Mieske, S., Zeilinger, W. W., & Chilingarian, I. 2013, *A&A*, 557, A21
- Saulder, C., van den Bosch, R. C. E., & Mieske, S. 2015, *A&A*, 578, A134
- Schombert, J. M. 1988, *ApJ*, 328, 475
- Sérsic, J. L. 1968, *Atlas de galaxias australes*
- Simard, L., Willmer, C. N. A., Vogt, N. P., et al. 2002, *ApJS*, 142, 1
- Sommer-Larsen, J., Romeo, A. D., & Portinari, L. 2005, *MNRAS*, 357, 478
- Sonnenfeld, A., Nipoti, C., & Treu, T. 2013, *ArXiv e-prints*
- Stockton, A., McGrath, E., Canalizo, G., Iye, M., & Maihara, T. 2008, *ApJ*, 672, 146
- Taylor, E. N., Franx, M., Glazebrook, K., et al. 2010, *ApJ*, 720, 723
- Terlevich, A. I., & Forbes, D. A. 2002, *MNRAS*, 330, 547
- Toft, S., van Dokkum, P., Franx, M., et al. 2007, *ApJ*, 671, 285
- Trager, S. C., Faber, S. M., Worthey, G., & González, J. J. 2000, *AJ*, 120, 165
- Tremblay, B., & Merritt, D. 1996, *AJ*, 111, 2243
- Trujillo, I., Cenarro, A. J., de Lorenzo-Cáceres, A., et al. 2009, *ApJ*, 692, L118
- Trujillo, I., Feulner, G., Goranova, Y., et al. 2006, *MNRAS*, 373, L36
- Valentinuzzi, T., Fritz, J., Poggianti, B. M., et al. 2010, *ApJ*, 712, 226
- van de Sande, J., Kriek, M., Franx, M., et al. 2011, *ApJ*, 736, L9
- van der Wel, A., Bell, E. F., Häußler, B., et al. 2012, *ApJS*, 203, 24
- van der Wel, A., Franx, M., van Dokkum, P. G., et al. 2014, *ApJ*, 788, 28
- van Dokkum, P. G., Franx, M., Kriek, M., et al. 2008, *ApJ*, 677, L5
- van Dokkum, P. G., Bezanson, R., van der Wel, A., et al. 2014, *ApJ*, 791, 45
- Vogelsberger, M., Genel, S., Springel, V., et al. 2014, *MNRAS*, 444, 1518
- Wake, D. A., van Dokkum, P. G., & Franx, M. 2012, *ApJ*, 751, L44
- Wellons, S., Torrey, P., Ma, C.-P., et al. 2016, *MNRAS*, 456, 1030
- Willman, B., Governato, F., Wadsley, J., & Quinn, T. 2004, *MNRAS*, 355, 159
- Yang, X., Mo, H. J., van den Bosch, F. C., et al. 2007, *ApJ*, 671, 153
- Zibetti, S., White, S. D. M., Schneider, D. P., & Brinkmann, J. 2005, *MNRAS*, 358, 949
- Zirm, A. W., van der Wel, A., Franx, M., et al. 2007, *ApJ*, 656, 66